AIAA JOURNAL
Vol. 32, No. 5, May 1994

Symmetry Breaking in Vortical Flows over Cones—Theory and Numerical Experiments

Peter M. Hartwich*
ViGYAN, Inc., Hampton, Virginia 23666

A stability analysis suggests that inviscid incompressible flow, independent from angle of attack and regardless whether attached or separated, over slender cones is only marginally stable in regions of decelerating circumferential flow. Reducing slenderness or surface curvature lowers the frequency spectrum of the harmonic perturbations and, thus, reduces their impact on the overall stability of flows over slender cones. Associating the notion of instabilities in such flows with the onset of vortex asymmetries provides a model for explaining a variety of flow phenomena in Navier-Stokes simulations of laminar (Re_l = 0.6, 1.2, and 2.4 × 10^6; l is body length) incompressible flows over three right circular cones [cone half-angle (δ) = 2.5, 5, and 10 deg] at moderate to high angles of attack (α/δ = 1, 2, and 3).

Introduction

ASYMMETRIC vortex shedding off slender bodies of continuously differentiable cross-sectional shape (e.g., cones, tangent ogives) occurs when such bodies are set at two to three times their nose half-angle.[1] The precise angle of attack for the onset of this phenomenon, also termed symmetry breaking,[2] depends on influence parameters such as body geometry (cross-sectional shape,[3] nose bluntness,[4] etc.), crossflow Mach number,[5] and Reynolds number.[6] Whereas extensive databases exist,[7–9] which can be compiled into useful guidelines for designing slender-nosed flight vehicles,[10] the key question about the origin of these asymmetries is still to be answered.

Several explanations have been offered as to the nature of symmetry breaking. In both wind-tunnel tests[8,11,12] and Navier-Stokes simulations,[12–14] a strong correlation was detected between surface imperfections and vortex-shedding events. This suggests symmetry breaking as the result of a convective instability. Consequently, symmetry breaking would have to subside once its source, some surface imperfection, is removed. This conclusion was indeed confirmed in experiment[12] and computation.[12,13] Still, there are some observations that are difficult to reconcile with the notion of convective instability. For example, hysteresis effects have been detected in experiments where asymmetric vortex flow patterns over slender bodies of revolution were mirror imaged by applying suction or blowing.[15,16] Moreover, several numerical results for supersonic inviscid conical flows over cones[17,18] suggested that vortex asymmetries arise "by themselves," triggered by minute perturbations introduced by, for instance, round-off errors. Extensions of such studies to viscous, locally conical flows over cones basically confirmed these results,[13,19] although some researchers found that the Reynolds number has to exceed a threshold below which viscosity would dampen out the effects of disturbances stemming from some sort of numerical noise (round-off errors, truncation errors, etc.).[13]

Some problems arose in attempts to carry these conclusions derived from the analyses for conical flows to fully three-dimensional flows over slender bodies of revolution with pointed nose tips. Space-marching solutions for supersonic flows over such configurations suggest that if the local Reynolds number at the cross-sectional stations close to the nose tip are subcritical then no asymmetries are observed over the remainder of the body.[13] Time-marching solutions for incompressible flows over a tangent-ogive cylinder indicate that symmetry breaking occurs even for subcritical sectional Reynolds numbers close to the apex.[14] This could be explained with the fact that time-marching solutions emulate the feedback effects present in computations of conical flows but absent in space-marching solutions. Either explanation though suffers from the fact that in the neighborhood of pointed nose tips the flow is three dimensional rather than conical.

This paper is aimed at breaking this deadlock by assuming that indeed hydrodynamic instabilities are the causative agent for symmetry breaking. To confirm or refute this working hypothesis, an attempt was made at identifying perturbations that could trigger hydrodynamic instabilities by applying a classical stability analysis to a simplified set of the Euler equations for incompressible flow over slender cones. Associating unstable or only neutrally stable flow with the onset of symmetry breaking, the results from this stability analysis are correlated with Navier-Stokes simulations of laminar incompressible flow over slender right circular cones with pointed as well as blunted nose tips at moderate to high angles of attack. Computational results rather than experimental data have been employed for these correlations because they allow for a faster and less expensive assessment of influencing parameters such as Reynolds number, cone shape, and nose radii, and they simultaneously yield detailed surface and off-surface flow information. These computations were carried out with an established implicit upwind method for computing three-dimensional incompressible flow.[20,21] The accuracy of the computed flowfield results was assessed by applying results from Hemsch's[22] similarity analysis, and numerical issues such as numerical dissipation, gridding, and boundary conditions are addressed.

Stability Analysis

A stability analysis is conducted for the Euler equations rather than for the Navier-Stokes equations. The decision to ignore viscous effects for the sake of a simpler mathematical problem can physically be justified by the assumption that dissipation will delay, not precipitate, disturbances. Moreover, as it was the case with the analysis of the "inviscid" Rayleigh equation instead of the "viscous" Orr-Sommerfeld equation to establish criteria for transition in boundary-layer flow, the present limitation of the stability analysis to inviscid flows was hoped to still yield some insight into the stability properties of the class of flows considered in this section.

With the assumption of incompressible flow (which decouples the energy equation from the equations for mass and momentum),

Received June 5, 1993; presented as Paper 93-3408 at the AIAA 11th Applied Aerodynamics Conference, Monterey, CA, Aug. 9–11, 1993; revision received Oct. 1, 1993; accepted for publication Oct. 14, 1993.

*Research Scientist, 30 Research Drive. Member AIAA.

the Euler equations for three-dimensional flow in cylindrical coordinates are

$$\begin{aligned} &u_r + (1/r)v_\theta + w_x + u/r = 0 \\ &u_t + uu_r + (v/r)u_\theta + wu_x - v^2/r = -p_r \\ &v_t + uv_r + (v/r)v_\theta + wv_x + uv/r = -(1/r)p_\theta \\ &w_t + uw_r + (v/r)w_\theta + ww_x = -p_x \end{aligned} \tag{1}$$

with r, θ, and x being the coordinates in radial, circumferential, and axial direction, and u, v, and w the respective velocity components. The velocity components are normalized with the freestream velocity V_∞, and r and x are nondimensionalized with some reference length l. The nondimensional time is $t = \tilde{t}\,(V_\infty/l)$, and $p = C_p/2$ (C_p is the pressure coefficient).

Assuming that the dependent variables describe some steady base flow with superimposed perturbations, that is,

$$\boldsymbol{Q} = \bar{\boldsymbol{Q}} + \boldsymbol{Q}' \tag{2}$$

with $\boldsymbol{Q}^T = (p, u, v, w)$ and $\bar{\boldsymbol{Q}}_t = 0$, and retaining only the terms linear in the disturbances, Eqs. (1) are rewritten as

$$\begin{aligned} &u'_r + (1/r)v'_\theta + w'_x + u'/r = 0 \\ &u'_t + u'\bar{u}_r + \bar{u}u'_r + (v'/r)\,\bar{u}_\theta + (\bar{v}/r)\,u'_\theta \\ &\quad + w'\bar{u}_x + \bar{w}u'_x - 2\bar{v}v'/r = -p'_r \\ &v'_t + u'\bar{v}_r + \bar{u}v'_r + (v'/r)\,\bar{v}_\theta + (\bar{v}/r)\,v'_\theta \\ &\quad + w'\bar{v}_x + \bar{w}v'_x - \bar{u}v'/r + u'\bar{v}/r = -(1/r)\,p'_\theta \\ &w'_t + u'\bar{w}_r + \bar{u}w'_r + (v'/r)\,\bar{w}_\theta + (\bar{v}/r)\,w'_\theta \\ &\quad + w'\bar{w}_x + \bar{w}w'_x = -p'_x \end{aligned} \tag{3}$$

In the spirit of a conical similarity (which is exact only for supersonic inviscid flow over conical bodies), the spatial dimensionality of Eqs. (3) is reduced by one through a coordinate transformation of the form $(r, \theta, x) \rightarrow (\xi, \theta)$ with $\xi = r/x$. This reduces Eqs. (3) in the neighborhood of slender bodies with $r(x)|_{\text{surface}} \ll x$ to

$$\begin{aligned} &\xi u'_\xi + v'_\theta + u' = 0 \\ &ru'_t + \xi u'\bar{u}_\xi + \xi\bar{u}u'_\xi + v'\bar{u}_\theta + \bar{v}u'_\theta - 2\bar{v}v' = -\xi p'_\xi \\ &rv'_t + \xi u'\bar{v}_\xi + \xi\bar{u}v'_\xi + v'\bar{v}_\theta + \bar{v}v'_\theta + \bar{u}v' + u'\bar{v} = -p'_\theta \end{aligned} \tag{4}$$

With $r(x)|_{\text{surface}} \ll x$ all quadratic terms in ξ have been neglected, and the momentum equation in axial direction has become decoupled from the remainder of the system of differential equations defined in Eqs. (4). Because of the time derivatives, Eqs. (4) still contain a length scale that prevents conical self-similarity; the equations may be thought of as locally conical as they describe a flow in the neighborhood of a slender cone that behaves like conical flow in the vicinity of an axial station $x = \text{const}$.

The continuity equation in Eqs. (4) is identically satisfied by a stream function $\psi'(\xi, \theta)$ with

$$u' = (1/\xi)\psi'_\theta \text{ and } v' = -\psi'_\xi \tag{5}$$

The pressure is eliminated from Eqs. (4) by forming a vorticity transport equation from the momentum equations:

$$\begin{aligned} &r\,(u'_\theta - \xi v'_\xi)_t + \xi u'\,(\bar{u}_\theta - \xi\bar{v}_\xi)_\xi + \xi\bar{u}\,(u'_\theta - \xi v'_\xi)_\xi \\ &\quad + v'\,(\bar{u}_\theta - \xi\bar{v}_\xi)_\theta + \bar{v}\,(u'_\theta - \xi v'_\xi)_\theta + \xi u'_\xi\,(\bar{u}_\theta - \xi\bar{v}_\xi) \\ &\quad + \xi\bar{u}_\xi\,(u'_\theta - \xi v'_\xi) + v'_\theta\,(\bar{u}_\theta - \xi\bar{v}_\xi) + \bar{v}_\theta\,(u'_\theta - \xi v'_\xi) \\ &\quad - \bar{v}_\theta v' - \bar{v}v'_\theta - \xi\bar{u}v'_\xi + u'\bar{v} - \xi u'\bar{v}_\xi = 0 \end{aligned} \tag{6}$$

Considering Eq. (6) along the body surface itself (where $\bar{u} = \bar{u}_\theta = u' = u'_\theta = 0$), rather than in its immediate vicinity, yields a form of Eq. (6) that can be analytically integrated:

$$r\xi\,(v'_\xi)_t + \bar{v}\xi\,(v'_\xi)_\theta + \bar{v}v'_\theta + [\xi\,(\bar{v}_\xi)_\theta + \bar{v}_\theta]\,v' = 0 \tag{7}$$

Note that terms such as $\xi\bar{u}_\xi$ and $\xi u'_\xi$ in Eqs. (6) have been eliminated from Eq. (7) by virtue of the continuity equation in Eqs. (4) and its equivalent for the base flow.

Next, assume the disturbances described by Eq. (7) to be caused by acoustic waves that propagate in time along radial lines with $\theta = \text{const}$ and $x = \text{const}$ toward or away from the body surface with wave fronts parallel to the surface contour. In the absence of viscosity, these acoustic waves can only be longitudinal waves with amplitudes in radial direction. Although these amplitudes have to vanish on the body surface itself, they will generate oscillations in circumferential direction along the inviscid body surface. The oscillations in circumferential direction are dictated by the continuity equation in Eqs. (4) and by the fact that u' and u'_θ are zero along the inviscid body surface, but not u'_ξ. Such disturbances are defined by

$$\Psi'(\xi, \theta, t) = \Phi(\theta)e^{i(\alpha\xi - \omega t)}, \qquad i = \sqrt{-1} \tag{8}$$

where Φ is a complex-valued amplitude and $(\alpha\xi - \omega t)$ the wave phase. For a complex-valued frequency $\omega = \omega_{\text{Re}} + i\omega_{\text{Im}}$, and a real-valued wave number α, Eq. (8) describes the amplification (for $\omega_{\text{Im}} > 0$) or damping (for $\omega_{\text{Im}} < 0$) of a perturbation $\Psi'(\xi, \theta, t)$ in time. If ω is real and α complex, Eq. (8) expresses the growth or decay of a disturbance in space. The respective real parts of the frequency and wave number describe sinusoidal waves. Since the goal of this stability analysis is to identify hydrodynamic rather than convective instabilities, only time-dependent disturbances are considered here.

Upon inserting Eq. (8), Eq. (7) assumes

$$\left[\frac{1}{\xi}\,(\xi\bar{v})_\xi - \bar{v}\xi\right]\Phi_\theta + i\alpha\bar{v}\Phi_\theta + i\left[\alpha^2\xi\omega r + \alpha\,(\xi\bar{v}_\theta)_\xi\right]\Phi = 0 \tag{9}$$

To determine which complex frequencies admit valid solutions to Eq. (9), the definitions for the complex amplitude and the complex frequency,

$$\begin{aligned} \Phi &= \Phi_{\text{Re}} + i\Phi_{\text{Im}} \\ \omega &= \omega_{\text{Re}} + i\omega_{\text{Im}} \end{aligned} \tag{10}$$

are inserted into Eq. (9). Multiplying the resulting equation with the conjugate complex amplitude

$$\Phi^* = \Phi_{\text{Re}} - i\Phi_{\text{Im}} \tag{11}$$

yields

$$\begin{aligned} &\left[\frac{1}{\xi}\,(\xi\bar{v}_\theta)_\xi - \bar{v}\xi\right][\Phi_{\text{Re}}(\Phi_{\text{Re}})_\theta + \Phi_{\text{Im}}(\Phi_{\text{Im}})_\theta] \\ &\quad - \alpha\bar{v}\,[\Phi_{\text{Re}}(\Phi_{\text{Im}})_\theta - \Phi_{\text{Im}}(\Phi_{\text{Re}})_\theta] - \alpha^2\xi\omega_{\text{Im}}r\,|\Phi|^2 \\ &\quad + i\left[\frac{1}{\xi}\,(\xi\bar{v}_\theta)_\xi - \bar{v}\xi\right][\Phi_{\text{Re}}(\Phi_{\text{Im}})_\theta - \Phi_{\text{Im}}(\Phi_{\text{Re}})_\theta] \\ &\quad + i\alpha\bar{v}\,[\Phi_{\text{Re}}(\Phi_{\text{Re}})_\theta - \Phi_{\text{Im}}(\Phi_{\text{Im}})_\theta] \\ &\quad + i[\alpha^2\xi\omega_{\text{Re}}r + \alpha\,(\xi\bar{v}_\theta)_\xi]\,|\Phi|^2 = 0 \end{aligned} \tag{12}$$

Adding to Eq. (12) its complex conjugate counterpart gives

$$\begin{aligned} &\left[\frac{1}{\xi}\,(\xi\bar{v}_\theta)_\xi - \bar{v}\xi\right][\Phi_{\text{Re}}(\Phi_{\text{Re}})_\theta + \Phi_{\text{Im}}(\Phi_{\text{Im}})_\theta] \\ &\quad - \alpha\bar{v}\,[\Phi_{\text{Re}}(\Phi_{\text{Im}})_\theta - \Phi_{\text{Im}}(\Phi_{\text{Re}})_\theta] \\ &\quad - \alpha^2\xi\omega_{\text{Im}}r\,|\Phi|^2 = 0 \end{aligned} \tag{13}$$

Assuming bilateral symmetry for the baseline flow and Φ_{Im} and Φ_{Re} to be of sinusoidal form, integration of Eq. (13) for $0 \le \tilde{\theta} \le 2\pi$ gives

$$\alpha^2 \xi \omega_{Im} r \int_0^{2\pi} |\Phi|^2 \, d\tilde{\theta} = 0 \tag{14}$$

that is, each but the last term in Eq. (13) vanishes separately through the just described integration. Subtracting from Eq. (12) its complex conjugate counterpart and applying to the resulting equation the same integration process that led to Eq. (14) yields

$$\int_0^{2\pi} [\alpha \xi \omega_{Re} r + (\xi \bar{v}_\theta)_\xi] |\Phi|^2 \, d\tilde{\theta} = 0 \tag{15}$$

According to Eqs. (14) and (15), Eq. (9) possesses only valid solutions for the real and imaginary components of the complex frequency ω satisfying

$$\omega_{Re} = -\frac{\bar{v}_\theta + \xi (\bar{v}_\xi)_\theta}{\alpha \xi r}$$
$$\omega_{Im} = 0 \tag{16}$$

Physically, this translates into either the complete absence of any perturbations or into the presence of neutral disturbances, that is, oscillations that neither grow nor decay in time.

Apart from practical considerations, the first interpretation is easily proven illusory. While imposing some constraints [physically meaningful solutions to Eq. (9) exist only for $\omega_{Re} > 0$, which requires as a necessary condition the simultaneous occurrence of decelerated circumferential flow and $(\bar{v}_\xi)_\theta < 0$], Eq. (16) states that ω_{Re} vanishes only in the limit of infinite bluntness (i.e., $\xi \to \infty$) or infinite surface curvature (i.e., $r^{-1} \to 0$). Thus, the linear system as encapsuled in Eq. (7) is neutrally or marginally stable, which means that its stability is only insured in the absence of nonlinear interactions between the baseline flow and some disturbances. Once nonlinear interactions occur, one intuitively expects the stability of the system to deteriorate as the frequency spectrum for ω_{Re} as defined in Eq. (16) grows. This means that oscillations may be expected to have more impact on the stability of a flow over a cone the closer they occur to the nose tip (i.e., $r \to 0$), or the more slender or quasi-two-dimensional in nature (i.e., $\xi \to 0$) the cone becomes. Let this section be closed by pointing out that the stability analysis was carried out without any assumptions as to the angle of attack or as to whether the surface flow pertains to attached or separated baseline flow.

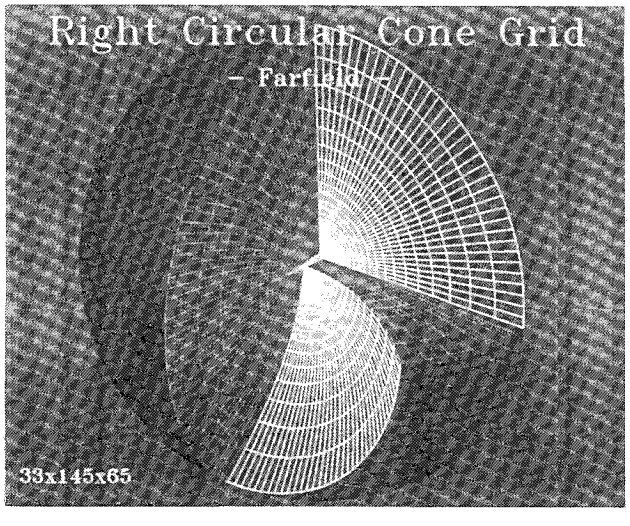

Fig. 1 Computational grid.

Numerical Approach

Governing Equations and Flow Solver

Although viscous effects were neglected in the stability analysis to simplify the mathematics, they are retained in the numerical experiments since, in practice, only separated flows are observed for slender cones at moderate to high angles of attack. Solving the Navier-Stokes equations facilitates a "natural" simulation of such flows with massive separation; in Euler solutions separation needs to be forced by specifying Kutta conditions, which carries the odor of being somewhat arbitrary in nature. Considering incompressible flow, as in the stability analysis, and using the same normalizations as in Eq. (1), the Navier-Stokes equations in their thin-layer approximation are written as

$$(\boldsymbol{Q}/J)_t + \boldsymbol{E}_\zeta + \boldsymbol{F}_\xi + (\boldsymbol{G} - \boldsymbol{G}_v)_\eta = 0 \tag{17}$$

The independent variables ζ, ξ, and η describe a curvilinear, body-fitted grid, with J being the Jacobian of the coordinate transformation. The solution vector bf $\boldsymbol{Q}$ comprises the pressure p and the three Cartesian velocity components u, v, and w. This reflects the use of Chorin's artificial compressibility concept,[23] which allows the solution of Eq. (17) in a coupled fashion with efficient time-marching algorithms originally developed for compressible flow.[20] The fluxes $\boldsymbol{E}$, $\boldsymbol{F}$, and $\boldsymbol{G}$ are the inviscid flux vectors. The viscous shear flux terms are lumped into $\boldsymbol{G}_v = \hat{\boldsymbol{G}}_v/(Re \cdot J)$, which means that viscous effects are accounted for only in the direction normal to the body surface. This simplification reduces the numerical expenditure without impeding accuracy for high-Reynolds-number application.[21] For the range of Reynolds numbers considered in this study, which focuses on the flow in the immediate vicinity of nose cone tips, it suffices to consider only laminar flow.[17,21,24]

Equation (17) is solved with a time-implicit upwind method called FMC1. Since details of the algorithm and code have been presented elsewhere (see Ref. 14, 20, and 21 and references cited therein), only its salient features are listed here. The upwinding of the inviscid fluxes is based on Roe's flux-difference splitting.[25] The viscous shear fluxes are centrally differenced. Grid-refinement studies indicated the overall accuracy of the spatial discretization to be of second order.[20] The solution of the discrete equations is advanced in time with a first-order accurate Euler-implicit procedure that employs approximate factorization in cross planes in conjunction with a symmetric planar Gauss-Seidel relaxation in the remaining spatial direction.

Body Geometry and Grids

Calculations are performed for pointed right circular cones with nose half-angles of 2.5, 5, and 10 deg and for right circular cones of 5-deg nose half-angle with blunted nose tips. The definition of the blunted nose tips is analytic with continuity through second derivative and, hence, curvature, and is given by

$$x(r) = a + br^2 \tag{18}$$

where r is the radius and with

$$a = 0.5 r_0 / \tan\delta \text{ and } b = (2 r_0 \tan\delta)^{-1} \tag{19}$$

which yields blunted nose tips with a nose radius of

$$r_{nose} = r_0 \tan\delta \tag{20}$$

where r_0 is the radius at the location where the blunting lets the surface contour deviate from that of a pointed right circular cone.

The flowfield results are computed on C-O-type grids (Fig. 1), which are generated by rotating in constant increments $\Delta\theta$ a two-dimensional C-type grid encompassing the contours of a right circular cone around its longitudinal axis. The outer contour of the integration domain (Fig. 1) is defined by a hemisphere with a radius of five cone lengths; earlier work on vortical flows over tangent-ogive cylinders[21] showed that such a grid extent should eliminate the effects of far-field boundary conditions on the flowfield solutions. The computations are predominantly carried out on grids

with $33 \times 145 \times 65$ points in longitudinal, circumferential, and radial directions, respectively. This grid density is comparable to that used in previous computations[14,21] to resolve laminar, transitional, and turbulent vortical flows over slender bodies of revolution. Those results in conjunction with spot checks on grid density effects in the present computational study give confidence that the laminar flows in the currently targeted Reynolds number range are sufficiently resolved. The radial stretching is defined by an increase in radial length from one mesh to another of 1.15; several flowfield results for varying stretching factors were obtained and proved insensitive toward variations of the stretching factor between 1.1 and 1.2. Grid points are bunched in the nose region by a cosine distribution of the surface nodes in the longitudinal direction. By virtue of Eq. (18), the resolution of blunted nose tips surpasses that of pointed nose tips.

Initial and Boundary Conditions

The computations are started from freestream conditions, meaning that all four flow variables are set to their freestream values except for $u = v = w = 0$ along the body surface. All boundaries are treated explicitly in time. Unfolding the physical domain (i.e., the C-O-type grid) into a regular computational domain described by a rectangular parallelepiped creates a radial branch cut and a polar singularity that extends like a boom of zero thickness from the nose tip all the way to the far-field boundary. Extrapolation with as well as without imposing bilateral symmetry is applied along the polar singularity. Both approaches were without any noticeable effect on the flowfield results. The radial branch cut was placed in the windward wind plane, and simple averaging of the extrapolates was used to update the solution there. Previous studies[14] indicated that neither the location of the branch cut nor any specific implementation of the continuity condition across these abutting boundary surfaces causes any discernible differences in the computed flowfield results. Along the cone surface, no-slip conditions are enforced in combination with a zeroth order extrapolation of the pressure.

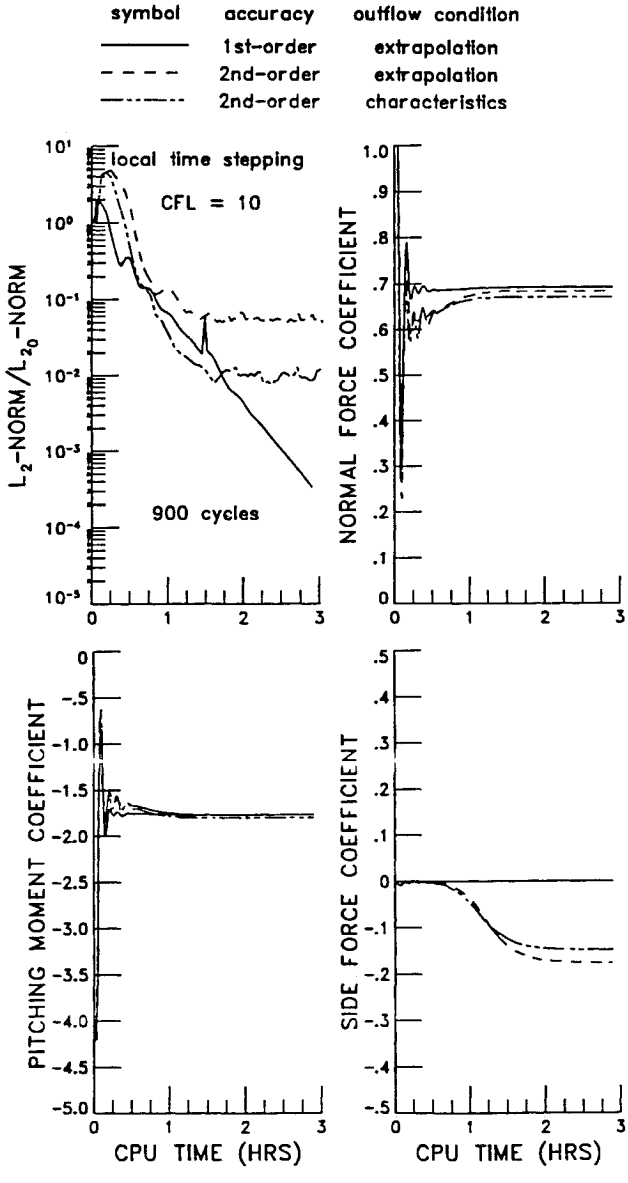

Fig. 2 Convergence summary for three computations of vortical flow over a cone: $\delta = 5$ deg, $\alpha = 15$ deg, $Re_l = 1.2 \times 10^6$, $33 \times 145 \times 65$ grid points.

Characteristic-based far-field conditions were used to promote convergence to steady state. Using Chorin's artificial compressibility concept,[23] neglecting viscosity in the far-field solution as well as all gradients tangential to the far-field boundary, and recalling that the Euler equations remain invariant under rotation produce the following characteristic equations:

$$\frac{d\hat{v}}{dt} = 0 \quad \text{along} \quad \frac{d\hat{x}}{dt} = \hat{u} \tag{21}$$

$$\frac{d\hat{w}}{dt} = 0 \quad \text{along} \quad \frac{d\hat{x}}{dt} = \hat{u} \tag{22}$$

$$\frac{dp}{dt} \pm \frac{\beta}{\hat{u} + \hat{S}} \frac{d\hat{u}}{dt} = 0 \quad \text{along} \quad \frac{d\hat{x}^{\pm}}{dt} = \hat{u} \pm \hat{S} \tag{23}$$

where $\hat{u}$ is the velocity component aligned with the unit vector $\boldsymbol{n}$ normal to the boundary, $\hat{v}$ and $\hat{w}$ are the velocity components tangential to the far-field boundary, β defines the amount of artificial compressibility, and $\hat{S} = \sqrt{\hat{u}^2 + \beta}$ corresponds to an artificial speed of sound. Integration of Eq. (23) yields

$$H_1 = p + [\hat{u}^2(1 - \hat{S}) - \beta \ell_n(\hat{u} + \hat{S})]/2 \tag{24}$$

$$H_2 = p + [\hat{u}^2(1 + \hat{S}) + \beta \ell_n(\hat{u} + \hat{S})]/2 \tag{25}$$

Equation (24) is evaluated at freestream conditions and Eq. (25) from extrapolation from the interior of the integration domain. Subtracting Eq. (24) from Eq. (25) yields an implicit expression for the normal velocity $\hat{u}$, which is solved iteratively. Once $\hat{u}$ has been updated, adding Eqs. (24) and (25) gives an equation for p. The Cartesian velocities $\boldsymbol{q} = (u, v, w)^T$ are determined on the outer boundary from

$$\boldsymbol{q} = \boldsymbol{q}_b + [\hat{u} - (\boldsymbol{n} \cdot \boldsymbol{q}_b)]\boldsymbol{n} \tag{26}$$

where the subscript b denotes freestream conditions for inflow or extrapolation from the interior for outflow.

These characteristic-based boundary conditions are also applied along the outflow cross plane. Alternatively, outflow conditions are specified from zeroth order extrapolation of all dependent variables. The impact of either formulation on the respective flowfield results is discussed next.

Results

Figures 2–5 address issues such as temporal and spatial convergence, boundary conditions, and physical correctness of the computed flowfield results. These results, together with pertinent remarks in the preceding sections of this paper and results from previous work on the validation of FMC1,[14,20,21] set the stage for correlating the results from the stability analysis with phenomena encountered in modeling viscous flows with vortices over pointed and blunted right circular cones.

Figure 2 demonstrates the impact of formal accuracy and of the formulation of the outflow boundary conditions on the temporal convergence of computations of laminar flow ($Re_l = 1.2$ million)

over a pointed right circular cone ($\delta = 5$ deg) at $\alpha = 15$ deg. Plotted are the L_2 norm of all four residuals, the normal force coefficient, the pitching moment coefficient (referenced with location of pointed nose tip), and the side force coefficient against CPU time. The timings are given for single-processor runs on a Cray Y-MP as installed at NASA Langley Research Center. The boundary conditions, except for the outflow conditions, were kept the same. All computations on the $33 \times 145 \times 65$ baseline grid produce closely matching values for normal force and pitching moment. Judged by the traces of the L_2 norm, the computations with first-order accurate upwinding of the inviscid flux terms, which introduces massive numerical damping, converged best, whereas the characteristic-based outflow conditions helped convergence for the higher-order accurate calculations. Apart from convergence aspects, Fig. 2 sheds light on the role of excessive numerical dissipation in simulating symmetry breaking. While the sizable side forces in the computations with the higher-order differencing are a telltale of vortex asymmetries, symmetry breaking is suppressed in the first-order accurate calculations as indicated by the absence of side force.

Whereas Fig. 2 has demonstrated the impact of the outflow boundary conditions on the convergence of the second-order accurate computations, Fig. 3 illustrates their effect on the computed flowfield results themselves. Figure 3 shows that the sectional normal force coefficients, normalized with local cross-sectional area,

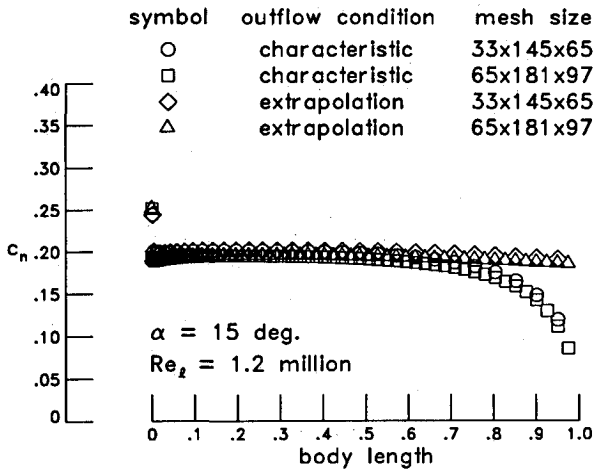

Fig. 3 Axial distribution of sectional normal force for a right circular cone: $\delta = 5$ deg.

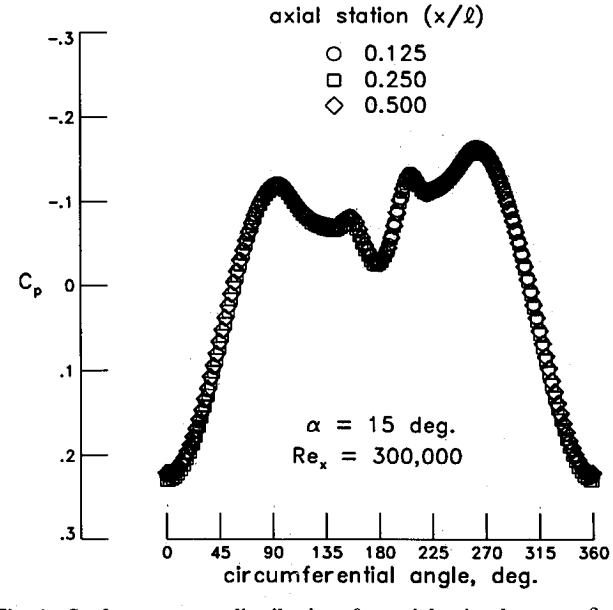

Fig. 4 Surface pressure distributions for a right circular cone: $\delta = 5$ deg, $33 \times 145 \times 65$ grid points.

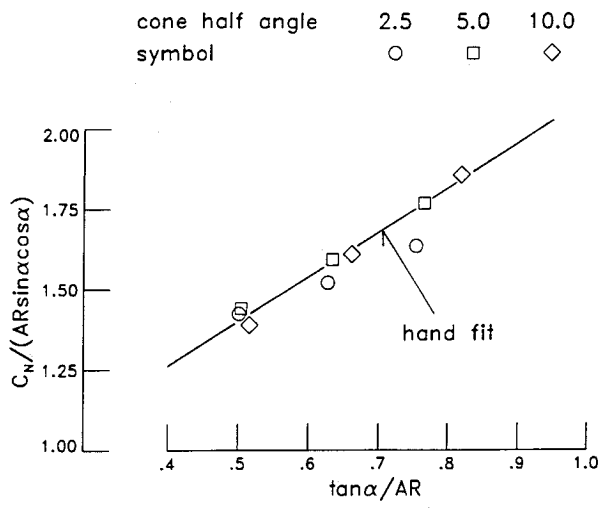

Fig. 5 Similarity correlations of normal force for right circular cones: $Re_l = 1.2 \times 10^6$, $33 \times 145 \times 65$ grid points.

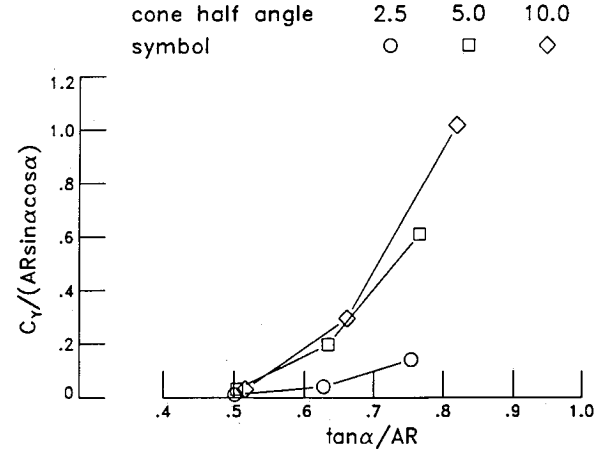

Fig. 6 Similarity correlations of side force for right circular cones: $Re_l = 1.2 \times 10^6$, $33 \times 145 \times 65$ grid points.

remain roughly constant for $0 < x/l < 0.6$ for either approximation of the outflow condition. This result holds true on the standard mesh with $33 \times 145 \times 65$ nodes as well as on an almost four times finer grid with $65 \times 181 \times 65$ nodes. Downstream of $x/l = 0.6$, the characteristic-based outflow conditions affect the flowfield solutions since they try to match the inner solution with external freestream conditions. To exclude the issue of downstream boundary conditions from the discussions of the computed flowfield results, the analyses of the Navier-Stokes solutions are restricted to $0 < x/l < 0.6$; this has already been practiced in creating Fig. 2 as it will be exercised throughout the remainder of the paper.

Figure 4 shows circumferential pressure distributions for second-order accurate calculations of asymmetric vortical flow over a circular cone ($\delta = 5$ deg) with $\alpha/\delta = 3$ and Reynolds numbers of $Re_l = 0.6$, 1.2, and 2.4×10^6. Since pointed cones are without any characteristic length, the unit Reynolds number has only a scaling effect. Figure 3 demonstrates that this viscous scaling effect is properly resolved on the standard mesh with $33 \times 145 \times 65$ nodes since the surface pressures for the same local axial Reynolds number (but for three different axial stations, with the shortest distance from the nose, x/l, corresponding to the highest unit Reynolds number Re_l) match very closely.

Hemsch's[22] work on the description of subsonic vortical flow over slender bodies using similarity parameters showed that the normal force is largely driven by aspect ratio and angle of attack with viscous effects playing a subordinate role. This result is used in Fig. 5 to validate the present flow simulations. Using Hemsch's

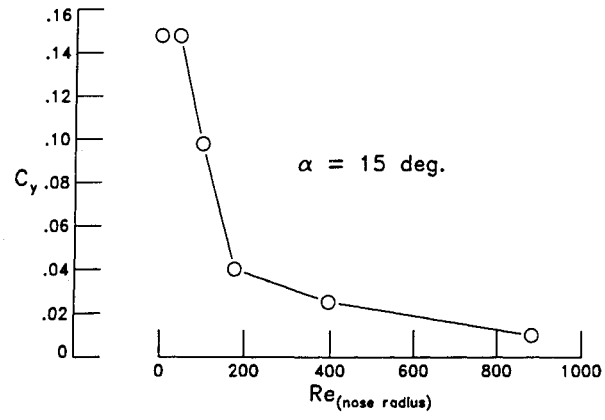

Fig. 7 Variation of side force with Reynolds number based on nose radius for a right circular cone: δ = 5 deg, 33 × 145 × 65 grid points.

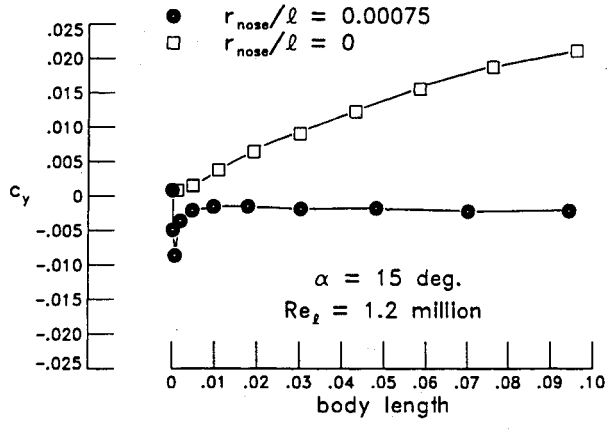

Fig. 8 Axial distribution of sectional side force in the nose regime of a blunted and a pointed right circular cone: δ = 5 deg, 33 × 145 × 65 grid points.

similarity parameter tan α/*AR* (*AR*: aspect ratio, here 4 × tan δ), the normal force coefficients (with base area as reference area), normalized with aspect ratio and functions of the angle of attack, for three cones of different slenderness can be collapsed to a simple linear function for $2 \leq (\alpha/\delta) \leq 3$, in accordance with the results from Hemsch's slender-body similarity.

Similarity is only formally used in Fig. 6 to show the effect of cone half-angle and angle of attack on side force (which, again, is formed with the base area as reference area). This figure leads to three conclusions: 1) slender-body similarity fails in predicting side force since it is sensitive to viscous effects; 2) the amount of side force grows with increasing cone half-angle; and 3) the larger the cone half-angle, the higher the incidence needs to be for encountering symmetry breaking. The last result supports a conjecture based on the stability analysis and expressed in Eq. (16), namely, that increasing slenderness increases the susceptibility of regular flows to disturbances that might lead to symmetry breaking.

The nose radius of a blunted cone makes for a natural choice for a length scale in defining a Reynolds number. This is exploited in Fig. 7 to summarize the effect of nose blunting on the development of side force for right circular cones with δ = 5 deg. To interpret these results, assume a nominal Reynolds number of 1.2×10^6, based on cone length. Blunting the nose as defined by Eq. (20) with a nose radius of as little as 0.075% body length reduces side force by an order of magnitude. With the equivalent Reynolds number based on nose radius being 9×10^2, it follows that halfing the Reynolds number based on cone length requires doubling the nose radius to 0.15% body length to achieve the same reduction in side force, as it was actually observed in numerical experiments. This result can be interpreted in light of the result in Eq. (16) from the stability analysis, which states that a reduction in surface curvature ("staying away from a pointed nose tip") reduces the frequency spectrum of oscillations that might trigger symmetry breaking. Of course, this interpretation needs to be taken with a grain of salt, since the assumption of locally conical flow becomes invalid in the neighborhood of the apex.

Figure 8 gives some insight as to the impact of nose blunting on the flowfield solution in the vicinity of the nose tip by comparing the axial distribution of sectional side force for a blunted and a pointed circular cone over the first 10% body length. Whereas side force monotonically grows along the pointed cone, it switches sign (which is indicative of a vortex-shedding event), produces a pronounced spike, and recovers to a constant, almost zero, level for the blunted nose.

The computational flow visualizations in Figs. 9 and 10 illustrate the flow processes associated with the side force traces in Fig. 8. Figures 9 and 10 show cross-sectional helicity-density patterns superimposed on surface flow images for about the first 8% body length. Helicity density is defined as the scalar product of the local velocity and vorticity vectors. It simultaneously indicates orientation and magnitude of rotational flow, thus providing a viable tool for analyzing complex three-dimensional flow by means of a scalar quantity. For the pointed cone (Fig. 9), tracking the flow from the far end of the heavily magnified nose section upstream toward

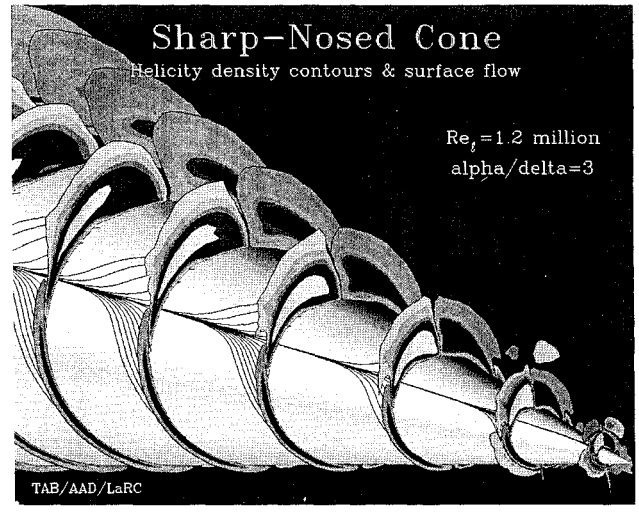

Fig. 9 Closeup of asymmetric vortical flow over a pointed right circular cone: δ = 5 deg, 33 × 145 × 65 grid points.

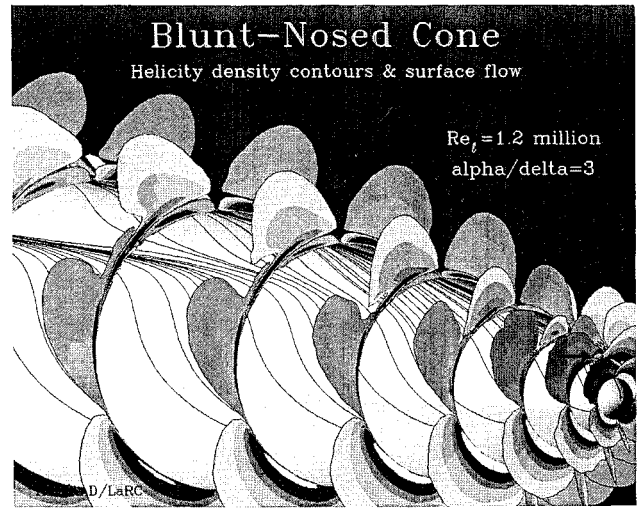

Fig. 10 Closeup of symmetric vortical flow over a right circular cone with a blunted nose cap: δ = 5 deg, 33 × 145 × 65 grid points.

the apex suggests that the starboard primary separation line as well as the vortex asymmetries extend all the way down to the nose tip. The flow right at the apex is elusive to flow visualization since the pertinent cross plane folds onto itself to form the aforementioned polar singularity.

The general impression of asymmetric vortical flow over a pointed cone being rather structured and straightforward is in quite some contrast to the flow patterns for the blunted cone in Fig. 10. The flow in the neighborhood of the blunted nose cap is attached, albeit highly rotational, as indicated by the helicity-density contours in the rightmost cross plane (which is the fourth axial grid plane in the integration domain). Stepping one crossflow station further downstream, the two leeside helicity-density patterns are separated by a small helicity-density "island" (highlighted by an arrow), indicative of an instability in the shear layer in the leeside wind plane. Looking at the third cross plane in the streamwise direction, this isolated instability spins off a pair of counter-rotating vortices that appear to sit on top of an attached leeside boundary-layer flow. Compared with the primary vortices in Fig. 9, these vortices are weaker, smaller in extent, and spaced farther apart from each other, and they remain almost perfectly symmetric. Moreover, they are not primary vortices that form only farther down the body as evidenced by the formation of a nascent starboard primary separation line.

As helpful as the results from the stability analysis were in explaining how reduced slenderness (cf. Fig. 6) and less surface curvature (see Fig. 7) delay symmetry breaking, one should keep in mind that the validity of these explanations hinges on the assumption that neutral oscillations, as predicted by the stability analysis, indeed trigger hydrodynamic instabilities that, in turn, lead to symmetry breaking. To demonstrate the correlation between such oscillations and symmetry breaking, surface pressures were monitored for asymmetric vortical flow over a pointed and for symmetrical vortical flow over a blunted ($r_{nose}/l = 0.00075$) right circular cone ($\delta = 5$ deg); in both cases, laminar flow with $Re_l = 1.2 \times 10^6$ was assumed, and α/δ was set to 3.

Figure 11 shows the variation of circumferential velocity along four circumferential grid lines 1, 3, 5, and 7 meshes off the cones surface at an axial station of about 1% body length. These antisymmetric velocity distributions pertain to a fully converged computation of symmetric vortical flow over a pointed cone where symmetry breaking was prevented by imposing bilateral symmetry. According to Fig. 11, the deceleration of the circumferential velocity components (i.e., $\bar{v}_\theta < 0$) and the decline of the radial change of their circumferential gradient [i.e., $(\bar{v}_\theta)_\xi < 0$, cf. Eq. (16)] are the steepest for $90 < \theta < 135$ deg and for $225 < \theta < 270$ deg. So, in accordance with Eq. (16), it is in these regions where the solution in Fig. 11 should be most prone to exhibit neutral oscillations (= amplitude constant with time).

Tracking the surface pressures in time at circumferential stations with $90 < \theta < 135$ deg and $225 < \theta < 270$ deg indeed indicated the presence of such perturbations. For a pointed cone, Fig.

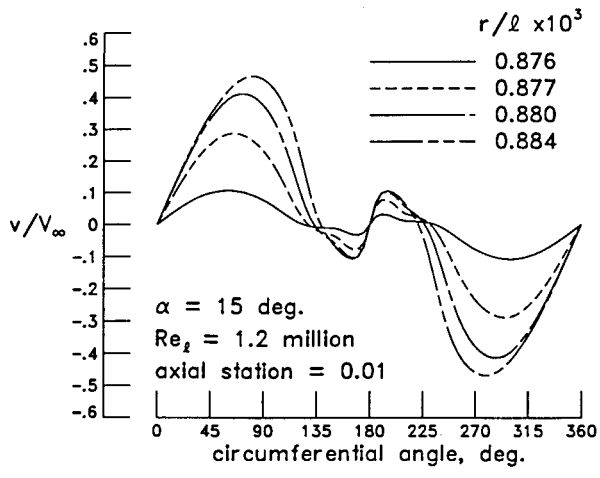

Fig. 11 Variation of circumferential velocity for a right circular cone: $\delta = 5$ deg, $33 \times 145 \times 65$ grid points.

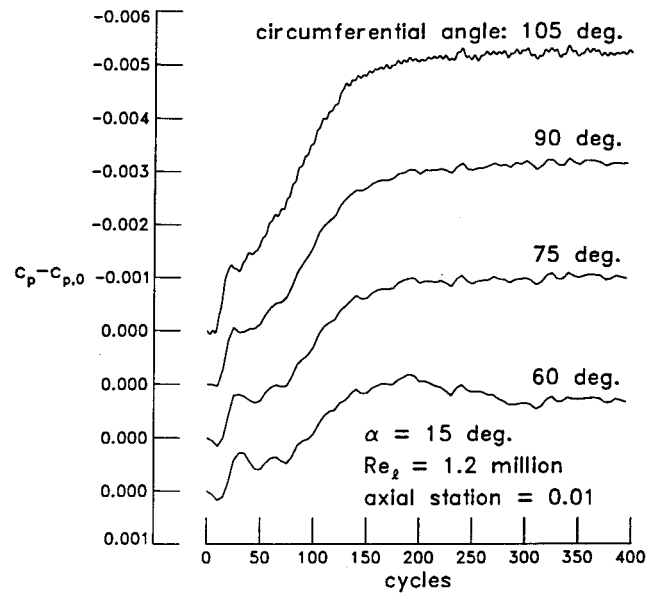

Fig. 12 Variation of surface pressure with time for a right circular cone: $\delta = 5$ deg, $33 \times 145 \times 65$ grid points.

12 shows the variation of surface pressure with the number of iterations after release of the bilateral-symmetry condition for four surface points along the starboard side of the cone. These spots are defined by their axial location (≈1% body length) and their circumferential angle ($\theta = 60, 75, 90$, and 105 deg). The shift in pressure level in all four traces reflects the occurrence of vortex asymmetries. The traces for $\theta = 60$, 75, and 90 deg exhibit pressure fluctuations that have already previously been observed for computations of vortical flows over tangent-ogive cylinders without symmetry breaking.[14,21] For $\theta = 105$ deg, these pressure fluctuations are superimposed by oscillations with almost an order of magnitude higher frequencies. The amplitudes of these higher-frequency oscillations stay roughly constant during the computations. Such high-frequency oscillations are absent in an analogous recording of the time history of the surface pressures for the blunted cone. These results appear to support the conjecture that the neutral oscillations trigger symmetry breaking. Unfortunately, the convincingness of this conclusion suffers from the fact that, for reasons of consistency and economy, all computations were carried out with local time stepping to promote convergence of the flow computations to solutions that, for engineering purposes, can be considered steady. Although one may argue that if truncation errors or round-off errors (the numerical source of hydrodynamic instabilities) trigger symmetry breaking, they will do so regardless of whether the computations are executed with global or local time stepping, it is undeniable that only computations using global time steps can truly mimic unsteady flow phenomena.

Conclusions

An application of classical stability analysis to inviscid incompressible flow over slender cones indicated that such flows are only neutrally stable. These results are valid for attached as well as separated flow at any angle of attack. The assumption that these perturbations build up and eventually trigger symmetry breaking provides a theoretical model to explain a variety of flow phenomena observed in Navier-Stokes simulations of vortical flows over slender right circular cones with pointed and blunted nose tips.

Acknowledgments

This work was supported by NASA under Contract NAS1-18585. The contributions by James M. Luckring and Robert M. Hall (both of NASA Langley Research Center) and Michael J. Hemsch (Lockheed Science and Engineering Company) in many fruitful discussions are gratefully acknowledged.

References

[1]Allen, H. J., and Perkins, E. W., "A Study of the Effects of Viscosity on Flow over Slender Inclined Bodies of Revolution," NACA TR 1048, 1951.

[2]Lowson, M. V., and Ponton, A. J. C., "Symmetry Breaking in Vortex Flows on Conical Bodies," *AIAA Journal*, Vol. 30, No. 6, 1992, pp. 1576–1583.

[3]Kegelman, J. T., and Roos, F. W., "Influence of Forebody Cross-Section Shape on Vortex Flowfield Structure at High Alpha," AIAA Paper 91-3250, Sept. 1991.

[4]Hunt, B. L., "Asymmetric Vortex Forces and Wakes on Slender Bodies," AIAA Paper 82-1336, Aug. 1982.

[5]Peake, D. J., and Owen, F. K., "Control of Forebody Three-Dimensional Flow Separation," AGARD-CP-262, Sept. 1979, pp. 15–46.

[6]Ericsson, L. E., "Sources of High Alpha Vortex Asymmetry at Zero Sideslip," *Journal of Aircraft*, Vol. 29, No. 6, 1992, pp. 1086–1090.

[7]Skow, A. M., and Erickson, G. E., "Modern Fighter Aircraft Design for High Angle-of-Attack Maneuvering," AGARD-LS-121, Paper 4, Dec. 1982.

[8]Keener, E. R., Chapman, G. T., Cohen, L., and Taleghani, J., "Side Forces on Forebodies at High Angles of Attack and Mach Numbers of 0.1 to 0.7: Two Tangent Ogives, Paraboloid, and Cone," NASA TM X-3438, Feb. 1977.

[9]Lamont, P. J., "The Effect of Reynolds Number on Normal and Side Forces on Ogive Cylinders at High Incidence," AIAA Paper 85-1799, Aug. 1985.

[10]Ericsson, L. E., and Reding, J. P., "Asymmetric Flow Separation and Vortex Shedding on Bodies of Revolution," *Tactical Missile Aerodynamics: General Topics*, edited by M. J. Hemsch, Vol. 141, Progress in Astronautics and Aeronautics, AIAA, Washington, DC, 1992, pp. 391–452.

[11]Moskovitz, C. A., Hall, R. M., and DeJarnette, F. R., "Effects of Surface Perturbations on the Asymmetric Vortex Flow over a Slender Body," AIAA Paper 88-0483, Jan. 1988.

[12]Degani, D., and Tobak, M., "Numerical, Experimental, and Theoretical Study of Convective Instability of Flows over Pointed Bodies at Incidence," AIAA Paper 91-0291, Jan. 1991.

[13]Thomas, J. L., "Reynolds Number Effects on Supersonic Asymmetrical Flows over a Cone at High Angle of Attack," *Journal of Aircraft*, Vol. 30, No. 4, 1993, pp. 488–498.

[14]Hartwich, P. M., Hall, R. M., and Hemsch, M. J., "Navier-Stokes Computations of Vortex Asymmetries Controlled by Small Surface Imperfections," *Journal of Spacecraft and Rockets*, Vol. 28, No. 2, 1991, pp. 258–264.

[15]Ng, T. T., and Malcolm, G. N., "Aerodynamic Control Using Forebody Blowing and Suction," AIAA Paper 91-0619, Jan. 1991.

[16]Bernhardt, J. E., and Williams, D. R., "The Effect of Reynolds Number on Vortex Asymmetry About Slender Bodies," *Physics of Fluids A*, Vol. 5, No. 2, 1993, pp. 291–293.

[17]Fiddes, S. P., "Separated Flows About Cones at Incidence—Theory and Experiment," *Studies of Vortex-Dominated Flows*, Springer-Verlag, New York, 1987, pp. 185–310.

[18]Marconi, F., "Asymmetric Separated Flows About Sharp Cones in a Supersonic Stream," *Lecture Notes in Physics*, Vol. 323, Springer-Verlag, New York, 1989, pp. 395–402.

[19]Siclari, M. J., and Marconi, F., "Computation of Navier-Stokes Solutions Exhibiting Asymmetric Vortices," *AIAA Journal*, Vol. 29, No. 1, 1991, pp. 32–42.

[20]Hartwich, P.-M., and Hsu, C.-H., "High Resolution Upwind Schemes for the Three-Dimensional, Incompressible Navier-Stokes Equations," *AIAA Journal*, Vol. 26, No. 11, 1988, pp. 1321–1328.

[21]Hartwich, P. M., and Hall, R. M., "Navier-Stokes Solutions for Vortical Flows over a Tangent-Ogive Cylinder," *AIAA Journal*, Vol. 28, No. 7, 1990, pp. 1171–1179; see also "Errata," *AIAA Journal*, Vol. 28, No. 10, 1990, pp. 1848, 1849.

[22]Hemsch, M. J., "Similarity for High-Angle-of-Attack Subsonic/Transonic Slender Body Aerodynamics," *Journal of Aircraft*, Vol. 26, No. 1, 1989, pp. 56–66.

[23]Chorin, A. J., "A Numerical Method for Solving Incompressible Viscous Flow Problems," *Journal of Computational Physics*, Vol. 2, No. 1, 1967, pp. 12–26.

[24]Bridges, D. H., and Hornung, H. G., "Effects of Tip Reynolds Number and Tip Asymmetry on Vortex Wakes of Axisymmetric Bodies at Various Angles of Attack," AIAA Paper 92-0406, Jan. 1992.

[25]Roe, P. L., "Approximate Riemann Solvers, Parameter Vectors, and Difference Schemes," *Journal of Computational Physics*, Vol. 43, No. 2, 1981, pp. 357–372.